J. Ind. Geophys. Union, 28(6) (2024), 385-403

***Invited Article***

# Evolution of Earth's upper mantle layers in the Magma Ocean Model

**Prashant Sharma[1,2]* and Ram S. Sharma[3]**
[1]Boston University, Department of Physics, 590 Commonwealth Ave., Boston, MA 02215, USA.
[2] Suffolk University, 8 Ashburton Place, Boston, MA 02108, USA.
[3] c/o Indian National Science Academy, Bahadur Shah Zafar Marg, New Delhi 110002, India
*Corresponding author: sharmap@bu.edu

## ABSTRACT

Planetary formation theory suggests that the Earth's upper mantle (UM) layers originated from a single silicate proto-mantle – a convecting magma ocean (MO). Because of the complexity of the gravitational instability of a solidifying magma ocean, numerical modeling studies have failed to show the formation of a chemically differentiated mantle that can be tectonically active. We present a hypothesis for the evolution of the upper mantle from the magma ocean state, consistent with the known experimental high-pressure studies on peridotitic melts. By theoretically analyzing the gravitational instability of the primordial upper mantle, we show that the peridotitic melt in the upper mantle crystallized to form cumulates of olivine, pyroxene, and garnet, creating a stable solid layer – the lithosphere at ~4.4 Ga. The remaining magma of basaltic composition, containing substantial Ca, Fe, and Al, separated into two parts – the silica-saturated mafic melt over the lithosphere and the olivine-containing dense mafic melt below. The surface melt crystallized and underwent partial melting by the heat flux from below, creating the TTG melt, thus giving rise to the early (~4.3 Ga) continental crust, which is now found in old cratons. We propose that the partial melting of the transition zone (TZ) material, emplaced at 220-250 km in the gravitational overturn process, created the asthenosphere. The coexisting melt ascended and accumulated below the lithosphere to form the Low-Velocity Zone (LVZ), and the unmoved restite formed the solid asthenosphere. The transformation of olivine into a spinel structure below 410 km and the perovskite structure at 660 km, formed the lower boundary of the upper mantle.

**Keywords**: Asthenosphere, Magma ocean, Lithosphere, Partial melting, Transition zone, Upper mantle

## INTRODUCTION

The Earth has gone through at least one episode of large-scale melting because of the Moon-forming impact at ~4.5 Ga (Tonks and Melosh, 1992; Reese and Solomatov, 2006; Carlson et al., 2014; Solomatov, 2015), or from the heat of planetary accretion, radio-decay, and core formation (Wood et al., 1970; Solomon, 1979; Wetherill, 1990). Gravitational differentiation of the molten proto-Earth into metals and silicates, led to the formation of the metallic core (dominantly Fe-Ni) and the silicate mantle. This primary silicate mantle melt is designated as the magma ocean (MO) (Abe, 1993; Solomatov and Stevenson, 1993; Drake, 2000; Solomatov 2015). The magma ocean's evolution to a layered convecting mantle remains an open problem (Korenaga, 2021). Theoretical and numerical analysis indicates that the magma ocean solidifies from the bottom up, and the cumulate layers grow progressively denser. The resulting gravitational instability resolves by a swift large-scale overturn. Such an overturn, however, leads to a stable stratified mantle that cannot support plate tectonics.

Here, we theoretically analyze the dynamics of gravitational overturn in a magma ocean model with a partial melt to a depth of (approximately) 400 km and a rheological transition to a solid below this depth. Using our theoretical treatment of the internal planetary physics and chemistry, we show that a partial melt in the upper mantle leads to small-scale gravitational overturns with well-separated timescales: The fast dynamics at shallow depths lead to the formation of the lithosphere and the crust; the slower dynamics at greater depth, create a more homogeneous asthenosphere and a zone of partial melt – the low-velocity zone. The density reversal due to overturn, changes the pressure profile of the upper mantle (UM), creating transition zone discontinuities. Thus, we identify the principal mechanisms of the magma ocean model that led to a layered and tectonically active upper mantle.

### Background

Theoretical and numerical analyses (Ballmer et al., 2017; Miyazaki and Korenaga, 2019; Korenaga 2021) suggest that the magma ocean solidification modes strongly influence the upper mantle's subsequent evolution. Numerical modeling, even with its limitations (Korenaga, 2021), has helped explore the role of magma ocean depth and crystallization mode in mantle evolution. A general assumption in these models is that the magma ocean (MO) is simply defined in the $MgO$-$FeO$-$SiO_2$ ternary system and that all liquids are lighter than the corresponding solids of $MgO$, $FeO$, $SiO_2$, and $MgSiO_3$ (Miyazaki and Korenaga, 2019). The depth at which the initial crystallization occurs in the magma ocean is determined by the intersection between the mantle adiabat and the pyrolytic liquidus (Solomatov, 2015). This initial point of crystallization may have ranged between the core-mantle boundary (CMB) and mid-mantle depth because the shapes of the liquidus and solidus (melting curves) of the pyrolytic mantle are not well constrained at depth (Bolrão et al., 2021). Accordingly, the existing theoretical and numerical modeling studies on magma ocean solidification are classified into two types: (A) magma ocean solidification from the CMB upward (Elkins-Tanton et al., 2003; Elkins-Tanton, 2008) and (B) magma ocean solidification originating at a mid-mantle depth and progressing toward the top and the bottom of the mantle (Labrosse et al., 2007; Mosenfelder et al., 2009; Bolrão et al., 2021).

In theoretical studies under type-A (for a review, see Elkins-Tanton, 2012), it has been argued that the primary magma ocean undergoes fractional crystallization from the CMB up, leading to gravitationally unstable density stratification due to the progressive enrichment of melts in iron. The gravitational instability leads to a large-scale overturn at the end of a relatively short magma ocean crystallization period (~Ma). During the overturn, the *Fe*-rich cumulate melt layer sinks to the core-mantle boundary (CMB). It remains stable as a highly dense layer at the base of the mantle, like the Large Low-Shear Velocity Provinces (LLSVPs) that seismological investigations have revealed. We note that in the MgO-FeO-$SiO_2$ ternary system, FeO-enriched melts are known to be significantly denser than coexisting solids (Ohtani et al., 1995; Nabiei et al., 2021). The LLSVPs explained by overturning in the magma ocean theory could also result from other reasons, for example, by the partial melting of the Archean mantle and the sinking of the resulting dense Fe-rich melts, subduction of early crust enriched with the delivered chondritic material; or trapping of Fe-Ni-S metallic liquids within the basal magma ocean (BMO) cumulates (Zhang et al., 2018). We show in this paper that gravitational overturns also redefine the pressure profile in the upper mantle (UM), leading to significant changes in the density stratification and the upper mantle structure.

In contrast to the type-A model, the type-B theoretical and numerical works (Labrosse et al., 2007; Stixrude et al., 2009; Caracas et al., 2019; Bolrão et al., 2021), considered several melting curves of mantle materials deduced from high-pressure melting experiments (Fiquet et al., 2010; Deng and Lee, 2017) , which suggest that solidification of magma ocean could begin from the mid-mantle region where the adiabat intersects the liquidus of the mantle, and crystals are neutrally buoyant (Mosenfelder et al., 2009; Caracas et al., 2019; Bolrão et al., 2021).

In the model of type-B, the accumulation of crystals with a high melting point at mid-mantle depth (ranging from ~ 100 GPa to about ~ 50 GPa, depending on the mode of crystallization) (Stixrude et al., 2009; Boukaré et al., 2015; Caracas et al., 2019), divides the magma ocean into two separate convecting regions (Bolrão et al., 2021): the top magma ocean (TMO) and bottom magma ocean (BMO). The TMO crystallization front moves upward (Bolrão et al., 2021), creating a *Fe*-rich cumulate-bearing melt layer on the top and gravitationally unstable stratification similar to that in type A models. The solidification of BMO has significant consequences for the composition of the lower mantle. Both experiments and simulations show that at lower mantle pressure, *Fe*-depleted crystals are buoyant in the coexisting *Fe*-enriched melt of the BMO (Boukaré et al., 2015; Nabiei et al., 2021) and likely to have formed approximately one-third of the lower mantle. Thus, *Fe*-enriched residual melt, with possible ferropericlase (FeO) crystallization, very likely forms a dense layer at the base of the mantle (Nabiei et al., 2021). These experimental conclusions are consistent with the observed seismic structure above the CMB, disclosing the presence of partially molten regions exhibiting composition differences with the overlying mantle (Garnero and McNamara, 2008). The high-pressure experiments on the pyrolite melt thus provide a petrological argument supporting early magma ocean crystallization and a stable Fe-rich melt layer near the CMB.

Having given a brief account of the theoretical and numerical modeling of the early Earth mantle, in the remainder of this paper, we focus only on the crystallization and solidification of the top layer of magma ocean (TMO) in the upper mantle (UM) since the crystallization of BMO is expected to occur over very long timescales (~ Ga) (Labrosse et al., 2007).

**Timescales of top magma ocean crystallization**

As mentioned above, the initial top magma ocean solidification proceeds from bottom to top in this magma domain (for both type-A and type-B models) since the mantle adiabat–the temperature profile of the stable melt–shows less change in temperature with depth (low lapse rate) than the liquidus (or the solidus). A rheological transition to a solid-like behavior occurs at a melt fraction of approximately 40% (Solomatov, 2015). The temperature gradient of such a partially crystallized magma ocean is approximately parallel to the solidus, leading to a superadiabatic temperature profile that makes the solidifying mantle gravitationally unstable. The instability grows much faster than the timescale for thermal diffusion. It is, therefore, treated as a *Rayleigh-Taylor* (RT) instability (Elkins-Tanton, 2012; Solomatov, 2015; Korenaga, 2021) that will lead to a gravitational overturn. The timescale for the overturn is (Turcotte and Schubert, 2002) $t_{RT} \approx 26\,\mu/gL\Delta\rho$, where μ is the viscosity of the solid mantle, $g$ is gravity, and $L$ is the length scale of the overturn across which there is a density contrast $\Delta\rho$. Early theoretical approaches (Elkins-Tanton, 2008, 2012; Solomatov, 2015; Santosh et al., 2017), focused on the chemical differentiation in the early stages of magma ocean fractional crystallization, not on the dynamics of the overturn. Since the rheological front and the closely following fuller solidification front grow rapidly in a vigorously convecting and cooling magma ocean, the onset of large-scale RT instability lags the rapid growth of the solidification front of magma ocean (expected to be completed in a period ~ka–Ma). Therefore, the overturn time was estimated (Elkins-Tanton, 2008) using the phenomenological expression for $t_{RT}$, which yields (for $L \approx 3000\,km$, a density contrast $\Delta\rho \approx 100\,kg/m^3$, and $\mu \sim 10^{19}\,\mathrm{Pa.s}$ ) $t_{RT} \sim Ma$. Recent numerical modeling of the dynamics of solidification and overturn (Ballmer et al., 2017; Maurice et al., 2017; Boukaré et al., 2018; Miyazaki and Korenaga, 2019), neglects details of chemical differentiation and focuses only on the primary determinants of gravitational instability–*Mg-Fe* exchange within the magma ocean. An essential outcome of these studies is that the RT instability grows in the form of multiple small-scale overturns (rather than a single large-scale overturn) during (not after) the magma ocean crystallization phase, with overturn timescales ranging from ~ka-Ma (Miyazaki and Korenaga, 2019), and Ma-0.1Ga (Ballmer et al., 2017; Bolrão et al., 2021), depending on the mantle viscosity used in these models. Therefore, the picture of a fully solidified and chemically differentiated magma ocean (formed in a period ~Ma) that subsequently undergoes large-scale overturn (Elkins-Tanton, 2008) is unlikely to be correct, which brings to question the chronology of the stable upper mantle layers that result from magma ocean crystallization. This question remains one of the more challenging aspects of the magma ocean model. Geochronological data are available only from the crust and indicate that the oceanic crust is young (<200 Ma), while the oldest known continental rocks found in a few cratonic regions are just over 4 Ga (Froude et al., 1983; Bowring and Williams, 1999; Harrison, 2009). The geochronology of other layers is unknown or uncertain, as the mantle materials brought to the surface by geological processes have undergone significant changes during and after their emplacement. Establishing the chronological evolution of the upper mantle layers is a complex and open problem.

In this paper, we propose a model for the formation of the four layers of the upper mantle, especially the lithosphere and the asthenosphere, which are components of the plate tectonic cycle, in a manner that is consistent with the existing petrological and geochemical evidence, and with the model of a crystallizing magma ocean. We also shed some light on the origin of the early (Hadean) crust, whose >4 Ga outcrops are found in a few cratonic regions of the Earth (Bowring and Williams, 1999; Harrison, 2009). Our model for the chronological evolution of the upper mantle layers, provides a framework for understanding the upper or top magma ocean (TMO) evolution during gravitational overturn. It extends the theoretical models of early Earth evolution (Elkins-Tanton, 2012; Solomatov, 2015; Bolrão et al., 2021; Korenaga, 2021) and bridges the gap between high-pressure experimental observations and the theory of the early Earth.

**Structure Formation in the Magma Ocean Model**

The solidus curve determines the boundary between the solid and the partial melt in the initial phase of magma ocean solidification (Elkins-Tanton, 2012; Solomatov, 2015; Ballmer et al., 2017; Miyazaki and Korenaga, 2019). Recent experiments indicate that the solidus curve of the Archean upper mantle was lower than estimated previously, making a partially melted layer deeper than 400 km very likely in the Hadean and early Archean times (Andrault et al., 2018). Therefore, it is reasonable to assume that when the magma ocean solidified from the bottom upward, there was a partial melt (melt fraction $\phi \approx 0.4$) at a depth of ≈400 km. The depth of the differentiated region below is from ~400 km to ~1000 km, with the melt fraction varying from zero at the bottom to ≈40% at the top (Solomatov, 2015). The magma ocean crystallization calculations (Elkins-Tanton, 2008) show that the early Earth (~4.5 Ga) partial melt layer ("mush"), is composed of crystals of olivine + clinopyroxene + orthopyroxene + garnet in a peridotitic melt. Below this mush layer, the solidified layers at depths $\gtrsim$ 400 km were: wadsleyite (40%)+ majorite (35%) + clinopyroxene (25%) up to 490 km; ringwoodite (45%) + majorite (55%) between 490 km and 600 km; and perovskite (95%) + wüstite (5%) below 600 km. Although this calculation is for the MgO-FeO-$SiO_2$ ternary system, one can generalize these conclusions to the FCMAS system that includes the mantle's significant components: FeO-CaO-MgO-$Al_2O_3$-$SiO_2$. This generalization is known to be important in the magma ocean theory of the mantle below 600 km (McFarlane et al., 1994; Solomatov, 2015) since any substantial segregation of perovskite crystals in the lower mantle would drive the ratios of minor and trace elements well outside of their observed range. Fractionation of small amounts of Ca-perovskite, in addition to Mg-perovskite, can increase the fractionation of perovskite (Liebske et al., 2005). More recent high-pressure experimental studies on pyrolite melt in the range of 52-129 GPa (Nabiei et al., 2021), also indicate that more than 33% of the pyrolytic magma ocean is likely to have crystallized the mineral bridgmanite (Bg, $MgSiO_3$) followed by the delayed crystallization of perovskite (Per, $CaSiO_3$) due to substantial solubility of Ca in bridgmanite.

**Modeling the magma ocean partial melt state and the RT instability**

In the magma ocean model, cooling due to vigorous convection leads to the formation of three zones: A liquid zone, where the temperature $T > T_{\text{liq}}$ (the liquidus temperature), a partial melt zone where the solidus temperature $T_{\text{sol}} < T < T_{\text{liq}}$, and a solid zone where $T < T_{\text{sol}}$ (Solomatov, 2015). Thermal cooling studies of the magma ocean also show the persistence of this trizonal mantle, with the upward migration of the partial melt region (where $T_{\text{sol}} < T < T_{\text{liq}}$), and the progressive shrinking of the liquid zone (Lebrun et al., 2013; Solomatov, 2015; Monteux et al., 2020). Composition-focused studies of the magma ocean model indicate that in the initial stage of magma ocean solidification, the *Fe*# (defined as the molar ratio $Fe\#/(Fe\# + Mg\#)$) in the top layer of the partial melt zone of the upper mantle is estimated to approach 1 in the fractional crystallization scenario (Elkins-Tanton, 2008; Ballmer et al., 2017). In other models (Miyazaki and Korenaga, 2019; Bolrão et al., 2021), *Fe*# is more limited ($\approx 0.3$). Regardless of the crystallization model, however, the *Fe/Mg* ratio decreases with increasing depth, creating a gravitationally unstable configuration. The RT instability arising from this superadiabatic thermal structure starts much before the solidification of the entire magma ocean and is of short wavelength (~0.1-100 km) (Ballmer et al., 2017; Maurice et al., 2017; Boukaré et al., 2018; Miyazaki and Korenaga, 2019). The time for the growth of short wavelength RT overturns ranges from ~ka (Miyazaki and Korenaga, 2019) to ~ Ma (Ballmer et al., 2017; Bolrão et al., 2021), and for a range of model parameters, even exceeds the unrealistic ~100 Ma (Ballmer et al., 2017). The timescale in these studies depends primarily on the value of mantle viscosity (ranging from $\sim 10^{19} - 10^{22}\ Pa.s$) and the thermal profile used in the models. Except for the ~100 Ma timescale scenario (an artifact of temperature and viscosity profile; Ballmer et al., 2017), the RT instability time in all models is much less than the thermal conduction time (~100 Ma). Together, these studies show that the evolution of the RT instability is dominated by short wavelength dynamics in the form of downwelling of iron-rich cumulate diapirs and upwelling of *Mg*-rich hot cumulates.

The growth of RT instability in the upper mantle when there is a sizeable partial melt layer above a solidified upper mantle, has not been analyzed in the existing literature. Such a mush layer, provides a viscosity contrast of several orders of magnitude since the viscosity μ decreases exponentially with the increase of melt fraction $\mu = \mu_s e^{-26\phi_m}$ (Mei et al., 2002). In existing calculations of RT instability, it is assumed that a layer of liquid overlies the solidified region. However, calculations of matrix compaction (Khazan, 2010), indicate that when the viscosity contrast between the matrix and melt is very high, the melt is distributed throughout the mush. We, therefore, model the upper mantle state resulting from fractional crystallization as a system with varying melt fraction and composition. To simplify the analysis, we consider a three-layer model with density decreasing from the top layer to the lower layers, because of compositional differences (primarily because of a decrease in Fe# with depth), while the viscosity increases because the lower layers have low ($\phi_m < 0.4$) melt fraction (see Figure 1a).

In *Methods-A*, we analyze the growth of the RT instability in a three-layer system like the upper mantle layering created by fractional crystallization (see Figure 1a). The top layer is *Fe*-rich with an average melt fraction much greater than 0.4, and the bottom layer is *Mg*-rich and solidified with an average melt fraction less than 0.4. The rheological transition is in the middle layer. As the *Methods-A* analysis shows, the gravitational instability grows several orders of magnitude faster in the top layer than in the bottom layer – the ratio of the growth rates being inversely proportional to the ratio of the layer viscosities. Therefore, small-scale overturns of such an upper mantle state proceed in two separate stages: The first stage (Stage 1) involves only the part of the upper mantle around $\approx 200$ km depth, while the second stage (Stage 2) involves the bottom portion of the upper mantle that develops much later. The overturn rate of the partial melt layer is estimated in *Methods-A* to be about four orders of magnitude faster than the overturn rate of the bottom portion of the upper mantle, and the separation in timescales of the two overturn stages ~ Ma.

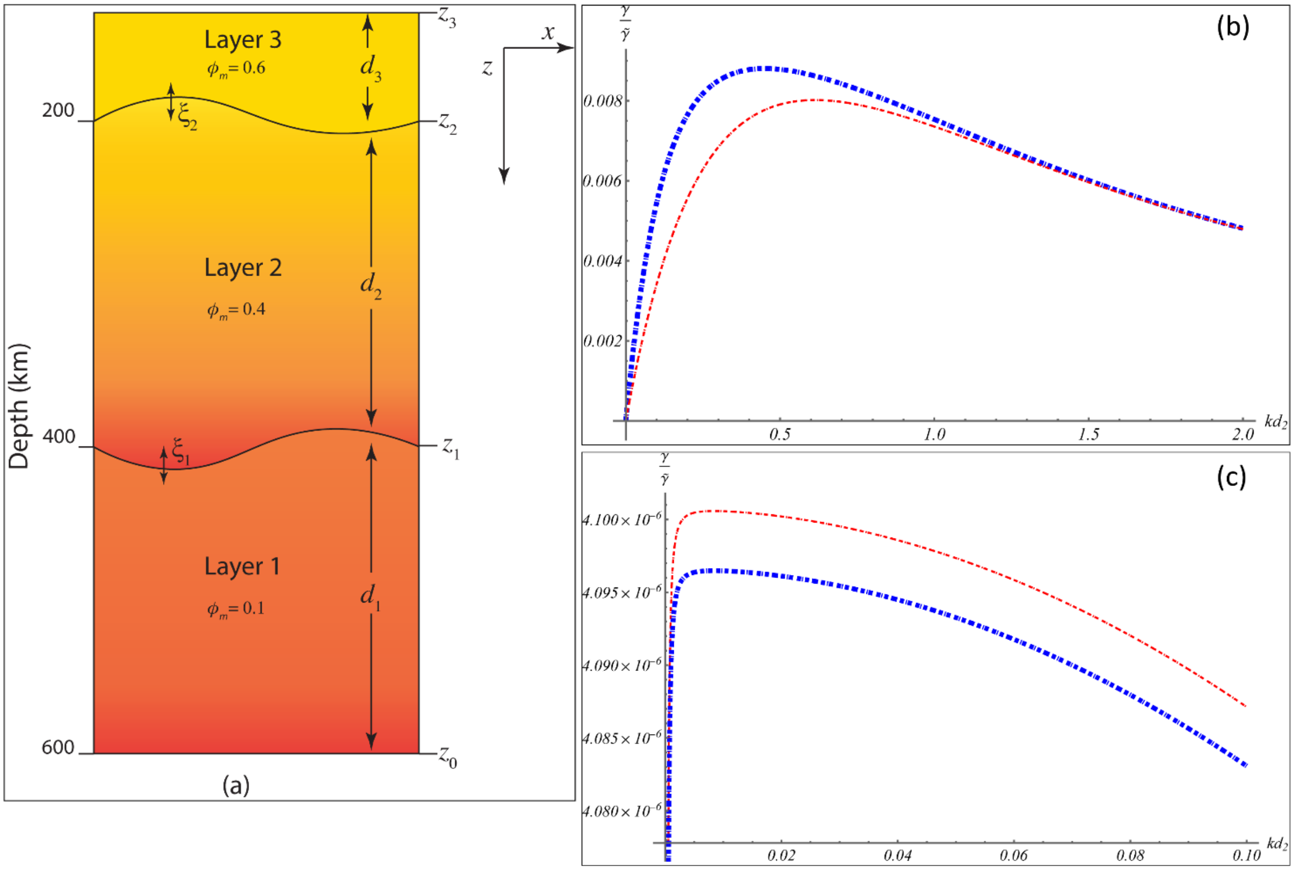


**Figure 1**. Three-layer model of Rayleigh-Taylor instability in the upper mantle. **(a)** The upper mantle is modeled as three distinct layers with different average melt fractions $\phi_m$. Each layer also has a fixed average density ($\rho_{i=1,2,3}$) and viscosity ($\mu_{i=1,2,3}$). A normal mode of the instability for both interface layers is schematically drawn, showing the vertical deviation ($\xi^{i=1,2}$) from equilibrium. **(b)** Dispersion relation for the top layer instability using the exact solution (dashed lines) of eqn. (2), and the approximate solution in the decoupled interface limit given by eqn. (3) (dotted lines) for $d_3/d_2 = 1/10,\ d_1/d_2 = 1.01$ (red colored thin lines), and $d_3/d_2 = 1/2,\ d_1/d_2 = 1$ (blue colored thicker lines). Note that the exact and approximate solutions (dashed and dotted lines) overlap. The growth rate scale $\tilde{\gamma} \equiv \rho_2\, g\, d_2/\mu_2$. **(c)** Dispersion relation for the bottom layer instability using the exact solution (dashed lines) of eqn. (2), which matches the approximate solution in the decoupled interface limit given by eqn. (3) (dotted lines) for $d_3/d_2 = 1/10,\ \ d_1/d_2 = 1.01$ (red colored thin lines), and $d_3/d_2 = 1/2,\ d_1/d_2 = 1$ (blue colored thicker lines).

The upwelling of *Mg*-rich hot cumulates to the upper layers of the mantle, and their decompression melting creates a *Mg*-rich melt in the top layer (≈ 200 km depth) of the upper mantle. The concurrent downwelling of *Fe*-rich melt through the upper mantle and its slow mixing with *Mg*-rich upwelling melt is expected to create a diverse range of melt compositions (Ballmer et al., 2017; Korenaga, 2021). We identify a range of *Mg*# compositions created in the partial melt layer–from *Mg*# 0.89 of the pyrolytic melt to *Mg*# 0.7–which we show below to be critical for the formation of a stable lithosphere layer.

**Proposed model for lithosphere evolution**

When the temperature of the partial melt (mush) layer drops below the liquidus, olivine crystallizes from the *Mg*-rich melt. This fractional crystallization will lead to unhindered grain growth due to Ostwald ripening, which should occur once the temperature of the entire layer falls below the liquidus (Solomatov, 2015). Experiments show that the melt-solid density crossover of olivine (forsterite, with Mg# ≥0.9) in a komatiitic (Stolper et al., 1981; Agee and Walker, 1993) melt is located in the range of 6-8 GPa (Agee and Walker, 1993; Ohtani et al., 1993, 1995) below ≈2000 C, depending on the compositional details. This range of pressure should occur at a depth range of 100–200 km (see *Methods-B* and Figure 2) in the early Earth.

For pressures higher than this density crossover, olivine is positively buoyant in the coexisting melt, leading to its accumulation around the neutral buoyancy depth of 100-200 km and the formation of the solid layer–the lithosphere.

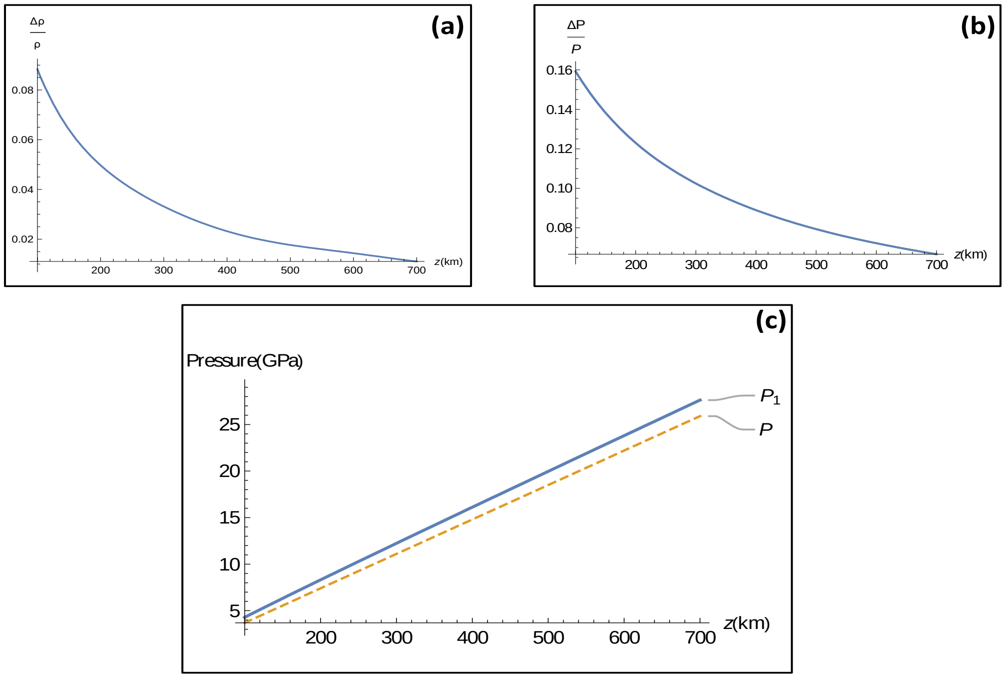


**Figure 2**. Pressure and density changes in the evolution of the magma ocean. **(a)** Fractional change in upper mantle density between the early solidified magma ocean (stage 1) and the more stable state with a well-defined upper mantle boundary (stage 2). The fractional change is calculated using the *Fe#* profile for fractional crystallization of the magma ocean. **(b)** Fractional change in pressure in the upper mantle between the early solidified magma ocean stage and the more stable state with a well-defined upper mantle boundary. The pressure is calculated using Eqn. (7) and the data from Figure 2(a). **(c)** Pressure $P_1$ in the upper mantle of the early solidified magma ocean (stage 1) and the linear pressure profile $P$ for the more stable state (stage 2).

Therefore, we propose that the *initial* lithosphere layer formed because of chemical heterogeneity (*Mg#* increasing with decreasing depth) of the upper layer ($\lesssim$ 300 km depth) of the mantle resulting from gravitational overturn. The initial lithosphere layer will likely be of variable thickness because of the lateral variation in *Mg#*. It separates the peridotite melt into an *Mg*-rich (*Mg#* 0.89) melt, lighter than the cumulate layer, and a denser, more *Fe*-rich (*Mg#*<0.77) melt below the bottom layer of the crystallized olivine. The denser melt contributes to the partial melt below (see *LVZ and the asthenosphere*). When *T* drops to ≈1800 C, orthopyroxene and garnet crystallize with olivine (Green and Ringwood, 1970; Wyllie, 1981; Fiquet et al., 2010; Lee et al., 2011). Thus, magmatic differentiation of the peridotitic melt at a depth of 100-200 km led to crystal settling of denser minerals, viz. olivine, orthopyroxene, and garnet, and formed the solid lithosphere layer (Figure 3a).

The proposed mechanism also indicates the composition of the early (Hadean) lithosphere. We note that the Archean lithosphere models (Ringwood, 1975; Herzberg and Rudnick, 2012), show compositions of forsterite olivine (75-80%, with *Mg#* 0.92-0.96), pyroxene (15-20%), and garnet (5-10%). The *Mg*-olivine with a forsterite component exceeding 75% indicates that the lithosphere is a cumulate and not a restite of mantle melting (Green and Ringwood, 1970; Wyllie, 1981). Being mafic in composition (*Mg#* 0.89), the melt in the upper layer of top magma ocean solidified to basalt (Figure 3b) upon cooling. This proposition finds support from the experimental works on the forsterite-diopside-silica ($Mg_2SiO_4$- $CaMgSi_2O_6$-$SiO_2$) system (Kushiro, 1969; Weng and Presnall, 2001), which show that mafic melts derived from pyrolytic/peridotitic mantle are separated into olivine-bearing mafic melt (Fo-En-Di) and silica saturated basaltic melt (Di-En-Qz) by a thermal divide due to the En-Di join, investigated at 2 GPa (Kushiro, 1969), and also at 5.1 GPa (Weng and Presnall, 2001) in the system (Cpx-Fo-Opx) (see Figure 4). If the mafic melt contains small amounts of *Al*, its crystallization will form minerals such as spinel and plagioclase. At depths greater than plagioclase stability, spinel is likely to react with pyroxene, giving rise to olivine and garnet by the following reaction, investigated experimentally at pressures of 2.5 GPa and *T* of 1400C (Takahashi, 1986).

$$\underset{\text{pyroxene}}{2Mg_2Si_2O_6} + \underset{\text{spinel}}{MgAl_2O_4} = \underset{\text{olivine}}{Mg_2SiO_4} + \underset{\text{garnet}}{Mg_3Al_2Si_3O_{12}}$$

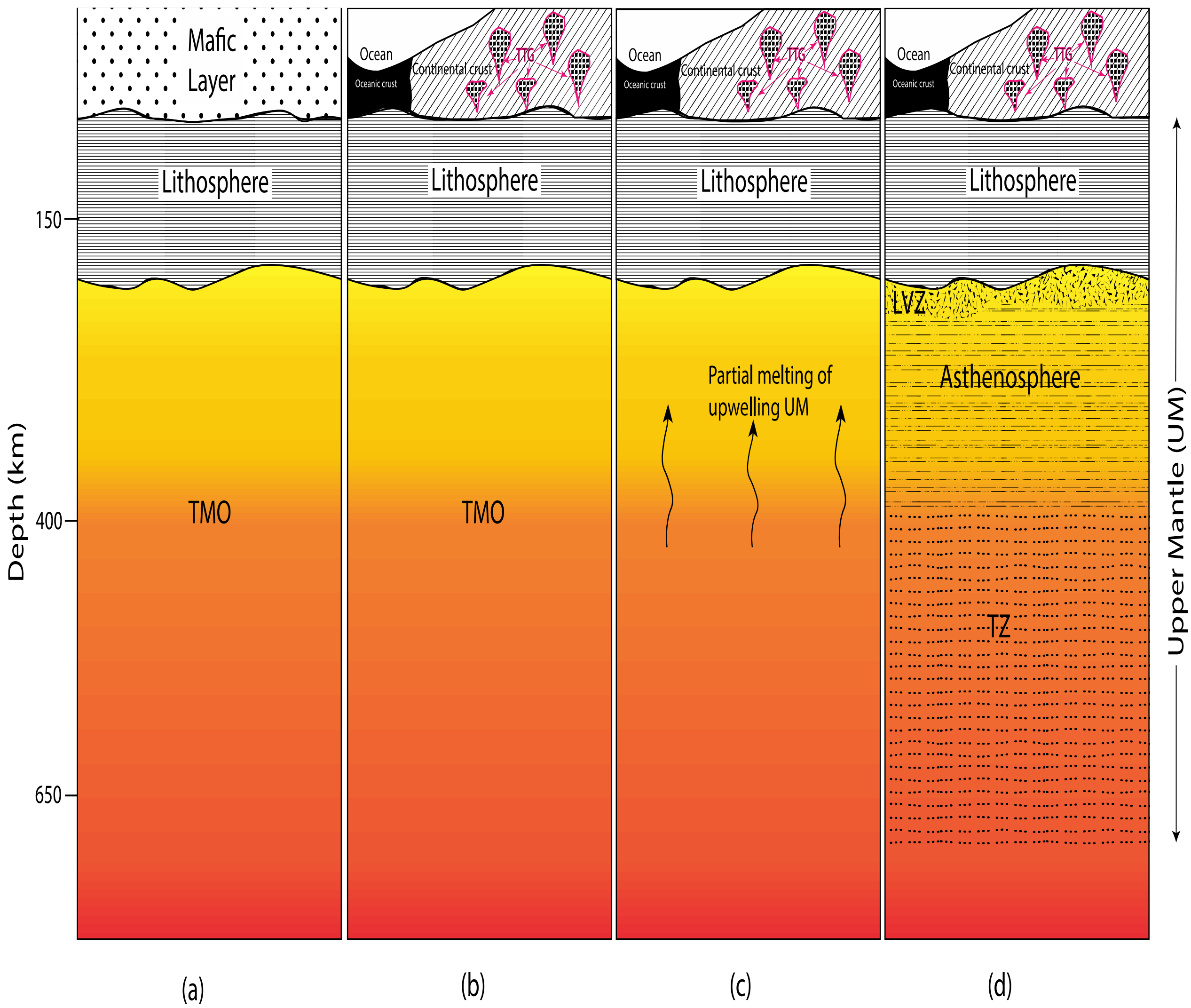


**Figure 3**. Gravitational overturn dynamics created compositional heterogeneity in the upper mantle (UM) due to the downwelling of *Fe*-rich diapirs and the consequent upwelling of *Mg*-rich cumulates. Viscosity variation with depth (depicted by lighter to darker shading in the figures) resulted in separate timescales for developing compositional changes in the shallower and deeper parts of the upper mantle. The resulting evolution of the upper mantle layers and Hadean crust are summarized diagrammatically in figures (a) through (d). (**a**) Fractional crystallization of the top magma ocean (TMO) generated cumulates of olivine, pyroxene, and garnet, collectively forming a rigid layer, the lithosphere—a garnet-peridotite layer. The leftover *Mg*-rich melt containing notable amounts of lithophile elements and *Na* solidified into a mafic layer resting over the lithosphere. (**b**) The mafic layer partially melted due to heat flux from below, generating a felsic melt of TTG, which now appear like diapirs intruding the variously altered metabasalt (greenstone). A thin mafic layer formed the oceanic crust resting over the oceanic lithosphere. (**c**) Upwelling of the solidified top magma ocean coupled with the topographic rise of the Hadean crust resulted in partial melting of the top magma ocean, whereby anatectic liquid ascended to accumulate below the lithosphere to form the LVZ, and the unmoved restite the asthenosphere. (**d**) Pressure due to overlying layers of the lithosphere, asthenosphere-LVZ, and the Hadean crust caused phase transitions at 410 km and 660 km depths, defining the top and bottom layers of the transition zone (TZ).

The product minerals of the reaction, namely, olivine, and garnet, are likely to add to the thickness of the already evolved lithosphere. A pertinent question arises regarding when the lithosphere formed in the Earth's evolution. Although lithosphere is formed even today in oceanic ridges, the earliest preserved lithosphere is in the 4030 Ma old Acasta Gneisses, NW Territories, Canada, and 3.85 Ga old Isua supracrustal rocks on Akilia Island in the Nuuk region of Greenland (Pilchin and Eppelbaum, 2008).

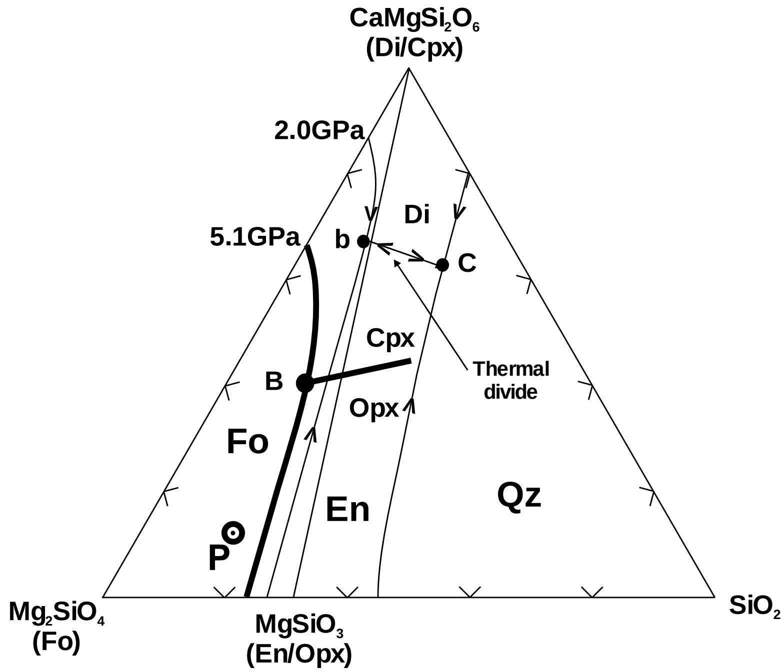


**Figure 4**. Forsterite (Fo)-Diopside (Di)-Silica (Qz) system at 2 GPa (after Kushiro, 1969) defining Di-Enstatite (En) divide between olivine-bearing mafic melt (subsystem Di-Fo-En, location *b*) and lighter mafic (basaltic) melt (subsystem Di-En-Qz, location *C*). The heavy solid line shows the liquidus phase relations and ternary eutectic (location B) in the clinopyroxene (Cpx)-Fo-orthopyroxene (Opx) system at 5.1 GPa (after (Weng and Presnall, 2001). Notice the shift of eutectic location *b* to location *B* with increasing pressure. Point *P* is the pyrolite mantle composition (Ringwood, 1975).

**Model for early mafic crust and TTG formation**

The silica-saturated mafic melt on the lithosphere was not only of lower density than the lithosphere but also the uppermost unit of the Earth's layer. Its cooling led to the formation of the early mafic crust of basaltic composition (Boyd, 1989; Dhuime et al., 2015). Soon after the gravitational overturn, the early Hadean Earth had significant atmospheric pressure, allowing erupting magmas to retain some volatile content as they solidified (Elkins-Tanton, 2008). At 100 bar pressure, lava can retain 1.0 wt.% water (Elkins-Tanton, 2008), implying that the earliest basaltic crust will have variable water content up to 1.0 wt.%. Therefore, we propose that in places where the early basaltic crust was considerably thick and more hydrous, it underwent partial melting because of the heat flux from below, leading to the development of droplets or blobs of felsic tonalite-trondhjemite-granodiorite (TTG) melt which ascended and assembled into large masses (Figure 3c). In contrast, the thin (and less hydrated) mafic layers that did not undergo partial melting became the oceanic crust resting on the oceanic lithosphere (Figures 3b-c) that later underwent subduction.

To estimate the thermal gradients needed for such a process of emplacement, we can model the ascent of the melt as a convective instability, for which a necessary condition (Landau and Lifshitz, 1987) is that the vertical temperature gradient of the melt exceeds the adiabatic gradient $g\alpha T/c_P$, where α is the thermal expansion coefficient, $c_P$ is the specific heat capacity, and $T$ is the average temperature of the melt, leading to a convective rise against gravitational acceleration $g$. Using granite solidus data (Sharma, 2016), we can obtain a reasonable estimate of the TTG melt temperature and specific heat. For a temperature of 1000 C (well above the melt temperature of 650 C), a thermal expansivity estimate of $3 \times 10^{-5}$ $C^{-1}$, and a specific heat capacity of 1100 J/kg C, we obtain a lower bound value of 0.35 C/km for the geothermal gradient associated with a typical TTG melt. Geothermal gradients for crustal depths are known to be much greater than this value. One may also consider the sufficiency condition for convective instability in a layer of fluid, which requires that the Rayleigh number of the viscous fluid layer exceed the critical Rayleigh number $\mathcal{R}a_c \approx 1708$ (Landau and Lifshitz, 1987). For a layer of thickness $h$, density $\rho$, kinematic viscosity $\nu \equiv \eta/\rho$, temperature difference ΔT, and thermal diffusivity $\kappa$, and Rayleigh number $\mathcal{R}a = g\alpha h^3 \Delta T/\nu\kappa$. Using the parameters for the lithosphere $h \approx 200\ km,\ \eta \approx 10^{19}–10^{21} Pa.s,\ \rho \approx 3 \times 10^3 kg/m^3,\ \kappa \approx 0.01\ cm^2/s,\ \Delta T \approx 1000\ C$, which are reasonable for a hot lithosphere with a granitic (tonalite) melt (Conrad and Molnar, 1997; Lev and Hager, 2008), we obtain the Rayleigh number $\mathcal{R}a \sim 10^6 - 10^4$, which is well above the critical limit.

Our proposal for TTG formation in the early crust is similar to the consensus on Archean TTG formation by partial melting of hydrated basaltic crust (Herzberg and Rudnick, 2012; Rozel et al., 2017). If the basaltic crust above the lithosphere contains enough amphibole, partial melting ensues by the heat flux from the mantle below. In the Hadean Earth, the heat flux could have been enhanced by the presence of short-lived radioactive isotopes, as suggested by Arndt (Arndt, 2013). The generated felsic melt was undoubtedly of TTG composition, as shown by the experimental studies on basaltic compositions (Moyen and Martin, 2012). The occurrence of TTGs within rocks of basaltic composition and the geochemical characterization of higher $Na_2O/K_2O$ and La/Yb and less-marked Eu anomalies (Taylor and McLennan, 1995; Kamber, 2015) strongly support the origin of TTGs by partial melting of the basaltic parent. Their low HREEs further suggest that partial melting of the mafic rocks occurred in the stability field of garnet (Kemp et al., 2010; Moyen and Martin, 2012; Kamber, 2015).

The proposed mechanism explains the lithosphere and early crust sequence and indicates how late Hadean granitic (TTG)-greenstone (meta-basalt) belts may have formed (Figures 3b-d) from a magma ocean model undergoing gravitational overturn. Examples of TTG domes are found in the Pilbara craton and many Eoarchean terranes (Kranendonk et al., 2007; Kranendonk, 2010). Partial melting may have occurred more than once to produce felsic magmas that crystallized the Jack Hills zircon (*cf*. Arndt, 2013).

Although the continental crust is chemically distinct from the underlying lithospheric mantle (subcontinental lithospheric mantle, SCLM), their association and similar ages suggest that its overlying crust followed the lithosphere formation, as evidenced by the presence of detrital zircons of 4.3-4.2 Ga age reported from Jack Hills, Narryer Complex, Western Australia (Hopkins et al., 2010). The 4.03 Ga old Acasta orthogneiss in the Superior Province of Canada (Bowring and Williams, 1999; Mojzsis et al., 2014) confirms the early crust formation at the Hadean time. The oldest known zircon from the Jack Hills, dated at $4.3 \mp 0.1$ Ga (Wilde et al., 2001), is considered to crystallize in felsic magma, indicating that the Earth had a solid crust for at least that long. Radiometric dating of the oldest Pilbara craton shows that the SCLM stabilized with the overlying early crust by 4.02 Ga (Wilde et al., 2001). Depletion of Na, Ca, and other lithophile elements and water in the lithosphere and the enrichment of these elements along with the radioactive heat-producing elements in the continental crust (Dixon et al., 2004) further support their origin nearly at the same time of ~4.4 Ga (Hopkins et al., 2010).

The early continental crust survived because it rested on the lithospheric mantle, which was more buoyant than the underlying mantle. However, erosion and meteoric bombardment during Hadean (~4.5 – 4.0 Ga) probably destroyed much of the early crust. Later, in the Archean, the TTG rocks underwent partial melting from the heat below, giving rise to intermediate rocks, followed by the widespread generation of K-granites with higher Rb/Sr ratios (Dhuime et al., 2015)–a change in composition that is associated with an increased crustal thickness (Hawkesworth et al., 2017).

## ORIGIN OF LVZ AND THE ASTHENOSPHERE

In the present-day mantle, below the solid lithosphere at a depth of 180–220 km from the surface, is the LVZ, a zone of low seismic velocities and high electrical conductivity. Because of its global occurrence, the LVZ cannot be explained by metamorphic or compositional variation and rheological changes. A plausible mechanism for its origin is the partial melting of upper mantle peridotite in the Earth's interior, aided by the ingress of water (Lambert and Wyllie, 1970; Mierdel et al., 2007; Hirschmann, 2010; Hua et al., 2023). An alternative mechanism that does not preclude partial melting requires enhanced water content in the thin LVZ layer (Karato, 2012). The presence of water in volcanic gases and hydrous minerals in mantle-derived inclusions implies that water is a constituent of the upper mantle (Philpotts and Ague, 2022). The experimental results also show that with 0.05 to 0.1 wt. % water, the garnet lherzolite (peridotite) melts at 2 – 3 GPa, or ca. 100 km in the mantle where the geotherm intersects the peridotite solidus (Wyllie, 1981; Fiquet et al., 2010). Thus, if the LVZ is a layer of partial melt with enhanced water content, its extent should depend on the steepness of the geotherm relative to the local solidus: a steeper geotherm (than the local solidus) will produce a thinner LVZ. At places where the geotherms do not intersect the local mantle solidus, there will be no LVZ, as is the case in some old cratons. The LVZ is predominantly found in the upper mantle at approximately 40 to 60 km depth beneath the oceanic lithosphere (Anderson, 2007).

Immediately below the LVZ is the 200 km-thick asthenosphere, a nearly homogenous solid, ductile layer modestly depleted in incompatible elements (Hofmann, 1988, 2007). These features of the asthenosphere and its low water content (Hirschmann, 2010) arise from the partial melting process that also contributes to the formation of the LVZ (Karato, 2012). Thus, the origin of the LVZ is coincident with the asthenosphere, and partial melting is a viable model for the origin of both the LVZ and the asthenosphere. Experiments reveal that the upper mantle at a depth of ~ 400 km contains $OH^-$ (water molecules) ranging from 0.05 to 0.1 wt. % (Hirschmann and Dasgupta, 2009).

Water at this depth is derived from crystals such as wadsleyite (Karato, 2012). Experiments have also shown that water storage in olivine reaches ~ 1000 ppm wt. $H_2O$ at 410 km depth (Férot and Bolfan-Casanova, 2012). Water can also be derived from a deep mantle in which the bulk $H_2O$ concentration is greater than the peridotite storage capacity, which *decreases* with decreasing depth (Hirschmann et al., 2005).

**Proposed mechanism for LVZ and asthenosphere formation**

We show here that in the magma ocean model, the Hadean Earth dynamics driven by gravitational instability, provide a mechanism for the formation of the asthenosphere and the LVZ. The dynamics of gravitational instability discussed above, consist of the downwelling of the dense *Fe*-rich diapirs originating from the top layer of the upper mantle and the upwelling of the *Mg*-rich bottom layers. The layers below $\approx 400\ km$ in the crystallization of the magma ocean are primarily composed of water-bearing wadsleyite and ringwoodite (Elkins-Tanton, 2008). We propose that the upwelling of these layers forced by the downwelling diapiric drips originating from the *Fe*-rich upper layers (<200 km depth) provides a natural mechanism for emplacement of the $OH^-$-bearing minerals (mainly wadsleyite and ringwoodite) from depths greater than 400 km to shallower depths of 220 – 250 km where the asthenosphere is now located.

The upwelling current is driven by *Fe*-rich diapiric drips whose size and descent velocity determine the broader background velocity of mantle upwelling. We model the diapiric drip as a Stokes flow whose descent time is linearly dependent on the mantle viscosity. The mantle viscosity in the magma ocean model increases with decreasing melt fraction and depth (Miyazaki and Korenaga, 2019). For a pyrolytic mantle at a melt fraction of 40%, the mantle viscosity $\eta_{mantle}{\sim}10^{14} Pa.s$ increases at a melt fraction of 10% to $\eta_{mantle}{\sim}10^{18} Pa.s$ (Miyazaki and Korenaga, 2019). Therefore, *Fe*-rich diapiric drips that originate in the shallower mantle depths will slow down considerably as they crossover into regions with melt fractions < 40% (at approximately 400 km depth). Accordingly, the upwelling of layers from below 400 km depth will occur at a timescale that is significantly (~$10^4$ times) longer than the formation of the lithosphere.

Using mass conservation, we estimate the velocity of the upwelling current originating from a layer of depth *L* located at radius *r* due to the downward flux of *Fe*-rich diapiric drips into the layer. Assuming that the diapirs are spherical and have a size (diameter) $d$, the downward mass flux of diapirs originating at radius $r$+$L$ across a boundary at radius $r$ is: $\rho \frac{\pi}{6} d^3 n_d v_d / L$, where $v_d$ is the downward diapir velocity, $n_d$ is the number of diapirs, $L$ is the thickness of the upwelling layer, and $\rho$ is the density of *Fe*-rich diapiric material. Taking the dominant wavelength of the RT instability, $\lambda$, to determine the surface density of diapirs, we estimate the number of diapirs $n_d \approx 4\pi(r+L)^2/\lambda^2$. The upward mass flux due to mantle upwelling of material with density $\rho_0$ is $4\pi r^2 \rho_0 v_0$, where $v_0$ is the upwelling velocity. Mass conservation requires the balance of upward and downward fluxes, which relates the upwelling velocity to the diapiric velocity:

$$v_0 \approx \frac{\rho}{\rho_0}(1+L/r)^2 \frac{\pi\lambda}{6L} v_d,$$

where we have used the approximation $\lambda \approx d$. We thus see that because of the small factor $\frac{\pi\lambda}{6L}$, the upwelling mantle velocity is generally slightly smaller than the diapiric velocity. Taking $v_d = 2\Delta\rho g d^2/9\eta$, the terminal velocity of a sphere in a fluid with viscosity $\eta$ and density contrast $\Delta\rho$ (Landau and Lifshitz, 1987), allows us to compare the velocity at different depths. Disregarding the decrease in the diapir diameter with increasing depth in the upper mantle (Ballmer et al., 2017) and focusing only on the viscosity dependence, gives us a lower bound for the decrease in the $v_d$ (and $v_0$) with increasing depth. Since the mantle viscosity changes from $10^{14}$ Pa.s at a melt fraction of 40% to $10^{18}$ Pa.s at a melt fraction of 10% (Miyazaki and Korenaga, 2019), the upwelling velocity at greater depths is ~$10^4$ times smaller than the corresponding velocity at shallower depths. The slower dynamics of mantle upwelling of deeper (>400 km) layers, imply that the asthenosphere formed after the lithosphere. We can estimate the asthenosphere formation timescale by finding the time of ascent of the upwelling layer using the calculated speed of ascent $v_0$. For a density contrast $\Delta\rho{\sim}100$ kg/m$^3$, a mantle viscosity $\eta{\sim}10^{21}$ Pa.s, a diapir diameter $d{\sim}10$ km, and an ascent depth $d_2$~100 km, we find the timescale $d_2/v_0$~100 Ma.

**Mantle upwelling and consequences**

Mantle upwelling is a common phenomenon and not just on Earth. Even the topographic rise observed on Venus is attributed to mantle upwelling (Stofan et al., 1995). In the given context, mantle upwelling resulted in $P$ reduction and a decrease in the melting point of water-bearing minerals (mainly wadsleyite and ringwoodite) in the mantle peridotite. The water ingress into the surrounding rocks, caused partial melting of the transition zone (TZ) material at the emplaced depth of 200–250 km. Mantle upwelling will cause enhanced partial melting by releasing water from peridotitic rock, which has less water storage capacity than the bulk $H_2O$ concentration at TZ depth (Bolfan-Casanova, 2005). Because the $H_2O$ storage of peridotite decreases with decreasing pressure, mantle material ascending from 410 km (with 600 ppm $H_2O$) melts as water is released and ceases melting only when the water content of the system decreases to a level below the storage capacity (Hauri et al., 2006). It is important to note that melt productivity in the adiabatic upwelling of mantle material increases with upwelling height (Hirschmann et al., 1999) because of increasing departure from the near-solidus conditions at 410 km depth. Therefore, a significant amount of melt would be generated in the upwelling mantle at the shallower depths of 200-250 km rather than at 410 km. The melt, being more buoyant, would rise to appear as a conductive LVZ layer under the lithosphere whose impermeable assemblage becomes a barrier, trapping the melt (Figure 3c). The restite of this partial melting becomes the asthenosphere (~4.3 Ga). As the residual material of the partial melting at a depth of ca.220 km, the asthenosphere is composed of heavier elements (*Mg* and *Fe*) and has low water content (Sifré et al., 2014) (Figure 3d).

It is interesting to consider the significance of this mantle upwelling for the early lithosphere layer, which, as mentioned before, could display inhomogeneity in depth. In the absence of upwelling, the partial melt below the lithosphere would be as dry as the lithosphere and have similar viscosity. Upwelling currents of the partial melt would likely deform the early lithosphere. Therefore, the proposed mantle upwelling that gives rise to the asthenosphere is likely to be coupled with topographic deformations of the early crust (Figures 3c-d). As the partial melt below the lithosphere solidifies over time to form the asthenosphere, the hydrous LVZ layer provides the viscous contrast needed to start the slow Archean plate tectonics.

Finally, we note that in an earlier model for the origin of the asthenosphere (Karato, 2012), partial melting of the mantle is assumed to occur at a depth of 410 km. Partial melting at a depth of 410 km leads to the problem of emplacing the restite or residual material of the melt to shallower depths of 200-250 km since the restite is heavier than melt and should remain at the place of partial melting while the melt migrates. The mechanism of asthenosphere formation in the early Earth that we have proposed, resolves this discrepancy in a physically simple and plausible manner. Furthermore, since a plume gives rise to basaltic volcanism (intra-plate volcanism) puncturing the lithosphere, as in the Hawaiian island chain, the plume heads must have been contained below by the asthenosphere. In light of experimental studies showing that the first melt of garnet-lherzolite formed at 1670 C (Wyllie, 1981), the asthenosphere should behave as a refractory boundary layer for an ascending plume.

The mechanism presented above shows how the asthenosphere formed late from the mantle, after the evolution of the lithosphere and its overlying crust. This chronology implies that plate tectonic processes were non-operative until at least the late Hadean when the asthenosphere formed. We note that the onset of proto-plate-tectonics in Hadean and Eoarchean times has been suggested (Foley et al., 2014; Hyung and Jacobsen, 2020; Windley et al., 2021), although we do not have an "empirical backbone for ascertaining the changes in Earth's history during Hadean times" (Korenaga, 2021).

**Discontinuities of the Transition Zone (TZ)**

The principal seismological discontinuities in the upper mantle are due to the $\alpha$-olivine $\rightarrow\beta$-olivine and $\gamma$-spinel $\rightarrow$ perovskite + magnesiowüstite phase transformations (Poirier, 2000). The occurrences of these transformations are connected to the evolution of the upper mantle. As discussed above, the transition zone formed in the initial phase of magma ocean solidification was gravitationally unstable. Partial melting of the transitions zone gave rise to the LVZ and the asthenosphere at approximately 220-250 km depth. The convective evolution of this instability and the mantle upwelling, coupled with the topographic rise of the early (~4.3 Ga) TTG rocks, disrupted the transition zone (Figures 3c-d). Therefore, the $\alpha\rightarrow\beta$ olivine, and $\gamma$-spinel$\rightarrow Pv + MW$, phase transformations occurred uniformly in the upper mantle only after the formation of the asthenosphere.

The $\alpha\rightarrow\beta$ olivine transformation occurs at 410 km depth at a pressure of approximately 15 GPa (well-constrained by seismic observations) when olivine transforms to ß-spinel (wadsleyite) at a temperature of 1800 K (Fei et al., 1992; Poirier, 2000). This transformation defines the upper boundary of the transition zone (Grotzinger and Jordan, 2019). The phase transformation is exothermic (a positive Clapeyron slope) and associated with a density increase of 8% (Poirier, 2000). In the early Earth (<1 Ma), however, a pressure of 15 GPa occurs at a depth of $\approx$ 370 km (see *Methods-B*). Thus, the $\alpha\rightarrow\beta$ olivine phase transformation will likely occur at a shallower depth when the magma ocean solidifies. Furthermore, with increasing *Fe*#, this transition occurs at lower pressure (Poirier, 2000). Given the high Fe#

in the shallower depths of the solidifying magma ocean, the transition likely occurred at even shallower depths in the mantle. Because this depth (<400 km) was in the zone of partial melting, no structurally sharp seismic discontinuity linked to the $\alpha \rightarrow \beta$ olivine transition was likely to be present in the early Earth (≲1 Ma).

The other phase transformation, in which spinel-structured olivine changes to a perovskite structure having silicon in 6-fold coordination, occurs at a depth of 660 km when the pressure is 24 GPa and the temperature is 1900 K (Chudinovskikh and Boehler, 2001). Structurally, high pressure causes increased close packing of oxygen around each silicon atom, thereby increasing the mineral density by 10% (Ringwood, 1975). The transformation is endothermic (Clapeyron slope -2.8 MPa/K) (Ringwood, 1975; Poirier, 2000; Hirose, 2002). Although garnet ($Mg_3Al_2Si_3O_{12}$) persists across the $\alpha \rightarrow \beta$ olivine transition, at pressures of approximately 17–19 GPa and above approximately 2000 K, pyroxene undergoes a phase change to a garnet structure (with a 10% increase in density): $2Mg_2Si_2O_6 \rightarrow Mg_3(Mg,Si)Si_3O_{12}$ , where the (Mg, Si) group occupies the octahedral sites that aluminum would occupy in the more common form of garnet (Poirier, 2000). Garnet transforms into a perovskite structure at a pressure higher than 23 GPa, an exothermic phase transition (Poirier, 2000; Hirose, 2002). These transformations create the 660 km discontinuity –the lower boundary of the transition zone (Figure 2). In the early Earth, with a solidifying magma ocean (<1 Ma) and high Fe# in the upper mantle, 24 GPa pressure occurs at a depth of 605 km. The pressure at 660 km depth is 26 GPa (an increase of 7%) (see *Methods-B*). Thus, the transition zone was 6% smaller when the magma ocean first solidified than when it formed after the gravitational overturn. Put another way, the gravitational overturn led to a decrease in *Fe#*, thereby decreasing the density and increasing the size of the upper mantle.

## METHODS

### Methods A: Rayleigh-Taylor (RT) instability growth calculation

As discussed earlier, the fractional crystallization of the magma ocean from the bottom up leads to a stratified structure which we model as a three-layer system with density decreasing from the top layer to the lower layers, because of the compositional differences (primarily because of a decrease in Fe# with depth), while the viscosity increases because the lower layers have low melt fraction (see Figure 1a). Because iron is preferentially partitioned into the melt phase, the density (and *Fe#*) variation is related to melt fraction variation (Miyazaki and Korenaga, 2019). We show below that the fastest growth rate of the RT instability is of the top fluid layer interface, and the bottom interface growth rate is scaled down by the ratio of the viscosities of the fluid layers.

The problem of finding the growth rate of Rayleigh-Taylor (RT) fluid instability when the fluid density and viscosity vary with depth is solved here using the perturbative flow approximation (Mikaelian, 1996), which is known to yield the growth rate dispersion within about 10% of the exact numerical solution for the single interface problem. Here, we solve the varying density (and viscosity) case analytically using this approximation for three layers of fluid, each with a different viscosity and density. We derive the dependence of peak growth rate on the fluid parameters.

The equations that govern the dynamics of a viscous fluid in the incompressible limit are the fluid equation of motion, $\rho \frac{\partial \bar{\mathrm{v}}}{\partial \mathrm{t}} = \nabla \cdot \sigma + \vec{\mathrm{f}}$ , the incompressible fluid constraint $\nabla \cdot \vec{v} = 0$ , and the constitutive relations $\sigma_{ij} = -p\delta_{ij} + \mu \frac{1}{2}\left(\partial_i v_j + \partial_j v_i\right)$ (Chandrasekhar, 1961). The symbols $\sigma_{ij}$, $p$, $\vec{v}, \vec{f}$ denote the deviation from the equilibrium state of the viscous stress tensor, fluid pressure, fluid velocity, and the external gravitational force density acting on the fluid. In the model three-layer system (Figure 1a), the fluid viscosity μ only has inter-layer variation, and the vertical fluctuations of the two interfaces from the reference equilibrium state are denoted by $\xi^{1,2}$ . To linear order in perturbation theory, the velocity and interface fluctuation can be analyzed in terms of their normal modes whose dependence on the planar coordinate and time is of the form $exp(ikx + \gamma t)$ (Chandrasekhar, 1961). Thus, for example, the interface fluctuation $\xi \equiv \xi(z)e^{ikx}e^{\gamma t}$, where k is the horizontal wave-vector and γ is the growth rate. Although we have chosen a 2D geometry here for simplicity, our results also apply to 3D Cartesian geometry. As a result of the normal mode ansatz, $\frac{\partial^2 v_z}{\partial x^2} = -k^2 v_z$. We now introduce the approximation $\nabla^2 v_z = 0$ (Mikaelian, 1996; Piriz et al., 2006), which implies that $\frac{\partial^2 v_z}{\partial z^2} = -k^2 v_z$ . Using the normal modes ansatz in the fluid equation of motion, we obtain the following equation governing the evolution of the normal modes of stress and fluid velocity assembled as a

vector $\mathrm{V} \equiv \begin{pmatrix} \frac{\sigma_{zz}}{2\mu k} \\ v_z \end{pmatrix}$

$$\frac{d}{dz}\mathrm{V} = \Gamma + \mathrm{k}\mathrm{M}\mathrm{V} \qquad (1)$$

Here $\mathrm{M} = \begin{pmatrix} 0 & \frac{\mu}{\mu_2} + \frac{\rho\gamma}{2\mu_2 k^2} \\ \left(\frac{\mu}{\mu_2} + \frac{\rho\gamma}{2\mu_2 k^2}\right)^{-1} & 0 \end{pmatrix}$,

$\Gamma \equiv \begin{pmatrix} \frac{\delta\rho g}{2\mu_2 k} \\ 0 \end{pmatrix}$, $\mu_2$ is a reference viscosity (taken to be the middle layer viscosity), and $\delta\rho$ is the change in density.

Equation (1) can be integrated across any depth to relate the quantities above and below the depth. For our three-layer model, the normal stress is discontinuous across any interface because of the interfacial density jump (modeled by $\delta\rho(z) = (\rho(z) - \rho_i)\xi^i\delta(z - z_i)$ , where $\delta(z - z_i)$ is the Dirac delta function), while the vertical velocity component is continuous across the interface. Using the zero normal velocity boundary condition for both the top and the bottom boundaries of the three-layer model we obtain the following equation relating the normal component of velocity and the interfacial displacements at the two interfaces $z = z_1$, and $z = z_2$:

$$\Phi \cdot \mathbf{v} = \Omega \cdot \xi \qquad (2)$$

where the velocity column vector $\mathbf{v} \equiv \begin{pmatrix} v_z^1 \\ v_z^2 \end{pmatrix}$, the interface displacement $\xi \equiv \begin{pmatrix} \xi^1 \\ \xi^2 \end{pmatrix}$, the matrices

$$\Phi \equiv \begin{pmatrix} \frac{\coth(kd_1)}{\coth(kd_3)}\frac{\mu_1^*}{\mu_2^*} + \frac{\coth(kd_2)}{\coth(kd_3)} & \frac{\tanh(kd_3)}{\sinh(kd_2)} \\ \frac{\tanh(kd_3)}{\sinh(kd_2)} & \frac{\mu_3^*}{\mu_2^*} + \frac{\coth(kd_2)}{\coth(kd_3)} \end{pmatrix}$$

$$\Omega \equiv \begin{pmatrix} \frac{(\rho_2-\rho_1)g\tanh(kd_3)}{2k\mu_2^*} & 0 \\ 0 & \frac{(\rho_3-\rho_2)g\tanh(kd_3)}{2k\mu_2^*} \end{pmatrix}$$

and $\mu_{1,2,3}^* \equiv \mu_{1,2,3} + \frac{\rho_{1,2,3}\gamma}{2k^2}$.

Since the normal mode of the vertical velocity at the i-th interface $v_z^i = \frac{\partial \xi^i}{\partial t} = \gamma\xi^i$ , we can rewrite the above equation (2) as an eigenvalue problem for the growth rate $\gamma$. In general, the condition $\det(\gamma\Phi - \Omega) = 0$ yields a quartic equation for $\gamma$, however, when $d_3/d_2 \ll 1$ we can neglect the coupling between the fluid interfaces (off-diagonal terms in the matrix $\Phi$) and obtain two quadratic equations that determine the interface instability growth rate as a function of the horizontal wave vector k. We thus find the analytical expression for dispersion for the RT instability of the top ($j = 3$) and bottom ($j = 1$) interfaces:

$$\gamma_j = \nu_2\, k \left( \sqrt{\psi_j^2 k^2 + \varphi_j \frac{\widetilde{\gamma_j}}{\nu_2}} - \psi_j k \right) \qquad (3)$$

Here the two frequency scales are $\widetilde{\gamma_3} \equiv (\rho_3 - \rho_2)gd_2/\mu_2$, and $\widetilde{\gamma_1} \equiv (\rho_2 - \rho_1)gd_2/\mu_2$ ; and

$$\varphi_j \equiv \frac{\tanh(kd_j)\tanh(kd_2)}{kd_2\left(\tanh(kd_j) + \frac{\rho_j}{\rho_2}\tanh(kd_2)\right)},$$

$$\psi_j \equiv \frac{\tanh(kd_j) + \frac{\mu_j}{\mu_2}\tanh(kd_2)}{\tanh(kd_j) + \frac{\rho_j}{\rho_2}\tanh(kd_2)};$$

and $\nu_2 \equiv \frac{\mu_2}{\rho_2}$ is the kinematic viscosity of the middle layer. Using Eqn. (3) we find an approximate expression for the peak growth rates: $\gamma_3^* \approx \frac{(\rho_3-\rho_2)gd_2}{2\mu_2\left(1+\frac{\mu_3 d_2}{\mu_2 d_3}\right)}$ (for the interface at $z = z_2$), and $\gamma_1^* \approx \frac{(\rho_2-\rho_1)gd_2}{2\mu_2\left(1+\frac{\mu_1 d_2}{\mu_2 d_1}\right)}$ for the bottom interface (at $z = z_1$).

For the case $\frac{\mu_3}{d_3} \ll \frac{\mu_2}{d_2} \ll \frac{\mu_1}{d_1}$, relevant to the initial state of the upper mantle near the rheological transition zone, we find the peak growth rates $\gamma_1^* \approx \frac{(\rho_2-\rho_1)gd_1}{\mu_1}$, and $\gamma_3^* \approx \frac{(\rho_3-\rho_2)gd_2}{\mu_2}$, such that

$$\gamma_1^* \ll \gamma_3^* \qquad (4)$$

We take the melt fraction to vary between 0.1 and 0.6 from the bottom layer to the top layer, with the middle layer melt fraction being 0.4, representing the rheological transition zone. Note that in the limit of large viscosity contrast between layers, the ratio of the growth rates $\gamma_3^*/\gamma_1^* \sim \mu_1/\mu_2$ only depends on the viscosity of the deeper solid layer and the viscosity at the rheological transition, not on the high melt fraction viscosity $\mu_3$. Using the exponential dependence of viscosity on the melt fraction (Mei et al., 2002; Miyazaki and Korenaga, 2019) $\mu = \mu_s e^{-26\Phi_m}$, the ratio of the viscosity of the bottom layer to the middle layer is $e^{7.8} \approx 3 \times 10^3$. Since the density varies primarily because of the change in *Fe#*, we can calculate the change in the density from one layer to another by using $\rho = \rho_0 + C\, x_{Fe}$ , where the constants are $\rho_0 = 4000$ kg m$^{-3}$, and $C = 850$ kg m$^{-3}$ (Ballmer et al., 2017). We choose the *Fe#* of the middle layer to be $x_{Fe} = 0.3$; *Fe#* of the top layer $x_{Fe} = 0.4$, and of the bottom layer $x_{Fe} = 0.2$, consistent with the $x_{Fe}$ variation found in Miyazaki and Korenaga (2019). Using these values, we plot the dispersion relation (Figures 1b-c) for both the exact and the decoupled interface limit for different values of $d_3/d_2$ showing that the decoupled limit is an excellent approximation for determining the dispersion relation even for comparable depths. We thus conclude that interface instability above the zone of rheological transition (melt fraction $\phi_m > 0.4$) grows much faster ($\gamma_3^*/\gamma_1^* \sim 10^4$) than the instability in the zone below the rheological transition (melt fraction $\phi_m < 0.4$). If we use $d_3 = 100$ km, $d_2 = d_1 = 200$ km, $\mu_s = 10^{22}$ Pa.s, we find the growth timescale for the upper layer instability to be $1/\gamma_3^* \approx 1$ ka, and the growth time scale for the instability of the lower layer $1/\gamma_1^* \approx$ 2 Ma.

An important consequence of the viscosity contrast between the layers above and below the rheological transition is that the RT instability rate of the topmost layer of the upper mantle is far greater than the instability rate of the layers below the zone of rheological transition. As discussed in the above sections, the topmost layer instability drives the lithosphere formation, which occurs at a much shorter time scale than the formation of the asthenosphere.

**Methods B: Pressure profile change calculation**

A feature of the bottom-up solidification of the magma ocean in early Earth is density reversal caused by excess Fe in the upper part of the solidifying magma ocean compared to the bottom. We will denote this as stage 1 of the evolution of upper mantle. Upon overturn, this excess Fe is distributed in the lower mantle (Elkins-Tanton, 2008; Ballmer et al., 2017), which is stage 2 of upper mantle evolution. Here we focus on an essential consequence of this density reversal: *a change in the pressure profile of the upper mantle*. A simple estimate of the change in density in the upper mantle results by considering the Fe/Mg dependence of the mineral densities crystallizing in the upper mantle. Using the data from Elkins-Tanton (Elkins-Tanton, 2008), for the mineral phases of olivine, pyroxene, spinel, garnet, wadsleyite, ringwoodite, majorite, perovskite, magnesiowustite, and post-perovskite, it is easy to see that there is a minimum increase in mineral density of 20% when *Fe#* increases to unity. Therefore, once the Rayleigh-Taylor instability-driven convections set in, the resulting decrease in *Fe#* in the upper mantle must result in decreased pressure in the upper mantle layers compared to the early stage of solidification. If, for example, the *Fe#* decreases from an average of 0.3 in the upper mantle layers (stage 1) to 0.1 (in stage 2), it should result in a change in (average) density of approximately 4%. However, because *Fe#* is not uniformly distributed in the upper mantle when the magma ocean first solidifies, the increased density (in stage 1 compared to stage 2) will be greater in the upper layers (<400 km depth) than in the lower portion of the upper mantle.

A more quantitative density (and pressure) profile of this change is obtained by using the data of the *Fe#* profile from the geodynamical modeling of the gravitational overturn, Ballmer et al. (2017). In a solidified upper mantle, the density profile is determined by *Fe#* (Ballmer et al., 2017):

$$Fe\# = \frac{Fe}{Fe+Mg} \quad (5)$$

Thus, upon determining the change in the *Fe#* profile in the upper mantle (between stages 1 and 2), $\Delta X_{Fe}$, the corresponding change in the density profile $\Delta\rho$ is evaluated (Figure 2a) using the relation given by (Ballmer et al., 2017)

$$\Delta\rho = C\ \Delta X_{Fe} \quad (6)$$

where $C = 850\ kg/m^3$.

Knowing $\Delta\rho$, the fractional change in the pressure $\Delta P/P$ (as a function of depth $z$) is computed (Figure 2b) by integrating the fundamental relation of hydrostatic equilibrium (Landau and Lifshitz, 1987):

$$d\Delta P = \Delta\rho\ g\ dz \quad (7)$$

Here, $dz$ represents the differential change in depth $z$. We note that this approach for determining the pressure for stage 1 contrasts with the method where the pressure is assumed to vary linearly with depth, and the densities of the crystallizing phases are determined based on the appropriate pressure and temperature for their positions in the mantle (Elkins-Tanton, 2008). However, such a linear pressure profile is appropriate for estimating the upper mantle pressure in stage 2, when the Fe# is a constant in the upper mantle. Therefore, for estimating the pressure in the upper mantle (in stage 2), we choose a linear pressure profile $P = 0.037 \times z$, which gives a pressure of 24 GPa at 660 km. Using the fractional change in pressure (Figure 2b), we obtain the pressure in the upper mantle during stage 1 of magma ocean solidification $P_1 = P(1 + \Delta P/P)$, as shown in Figure 2c. We find the depth $z \approx 605\ km$ at which $P_1$=24 GPa (Figure 2c). Thus, the 660 km discontinuity was at a significantly higher location in the early solidified magma ocean (< 1 Ma). The pressure of 15 GPa associated with the 410 km seismic discontinuity occurs in stage 1 of magma ocean evolution at a depth of 371 km. Similarly, we find that the pressure of 7.5 GPa, corresponding to the neutral buoyancy point of olivine in an *Mg*-rich (komatiitic) melt (Stolper et al., 1981; Agee and Walker, 1993), occurs at $z \approx 180$ km in the early solidified magma ocean, approximately 23 km higher than where it would occur in stage 2. Finally, we note that thermal profile changes between stages 1 and 2 would have an order of magnitude smaller effect on these conclusions because of the low thermal expansivity ($\alpha \approx 10^{-5}$/K) of the solidified upper mantle.

## DISCUSSION

Solidification of primordial magma ocean involves the growth of a crystallization front from the bottom up (Elkins-Tanton, 2008; Solomatov, 2015; Ballmer et al., 2017; Korenaga, 2021). Numerical studies have typically modeled the crystallization front as a sharp boundary between the solidified low melt fraction region and a "mush" or high melt fraction region. Since the high melt fraction region has the highest *Fe*#, such a model results in the entire density contrast confined to a narrow portion of the upper mantle—the crystallization front. Consequently, the dynamics of such a gravitational instability involve a single timescale determined by the viscosity of the solidified (low melt fraction) portion of the upper mantle. Such an approach is adequate for understanding how the gravitational overturn results in an almost complete reversal of *Fe*# distribution (Elkins-Tanton, 2008; Ballmer et al., 2017; Miyazaki and Korenaga, 2019; Korenaga 2021). However, this approach ignores the complexities arising from the variation in viscosity near the crystallization front. A careful treatment of the dynamics of the gravitational instability should consider the consequences of variations in melt fraction and composition for the evolution of the gravitational instability in the upper mantle.

Our three-layer model focuses on understanding the implications of melt fraction variation on the evolution of gravitational instability. It is essentially a 1D model and does not consider lateral heterogeneities. Experimental studies indicate that a partially melted layer about 400 km deep was very likely in the Hadean and early Archean times (Andrault et al., 2018). Therefore, it is imperative to understand the role of a partial melt in the evolution of the upper mantle. Based on thermodynamic studies of crystal accumulation in the solidifying magma ocean (Miyazaki and Korenaga, 2019), we model the density variation in the upper mantle by three layers, each layer having a different composition and melt fraction. There is a phenomenological relation between the viscosity and the melt fraction (Mei et al., 2002), which implies that a 10% variation in the melt fraction changes the viscosity by more than one order of magnitude. The three different melt fractions: $\phi_m = 0.1$ for the solidified upper mantle below 400 km; $\phi_m = 0.4$ for the portion of the upper mantle between 200 and 400 km; and $\phi_m = 0.6$ for the layer above 200 km, are representative of the discontinuous variation in melt fraction in a solidified upper mantle in the magma ocean model. In a multi-layered system, the interfaces with the largest density discontinuities will dominate the growth of gravitational instabilities. Therefore, even though we have only chosen three different density values, our conclusions should generalize to a continuous variation of melt fraction above the rheological front, and the model is a coarse-grained approximation of the upper mantle viscosity variations in the early mush stage of the magma ocean model. It allows us to derive analytic predictions for the growth of the Rayleigh-Taylor instability, showing that there are two widely separated growth rates in the problem of gravitational overturn of the upper mantle, which corresponds to the gravitational instabilities of the top and the bottom layers of our three-layer model (*Methods-A*). The two timescales are primarily determined by the middle and bottom layer viscosities. Since these layers have melt fractions that differ by 30%, the growth rates are four orders of magnitude apart. Furthermore, these growth rates are insensitive to our choice of the exact value of the melt fraction of the uppermost layer.

The faster growth rates and the lower viscosity of the upper layer led to rapid cumulate mixing and convective cooling and a consequent decrease in melt fraction (increase in viscosity). Thus, the fast overturn of the top layers ($\approx 200$ km depth) increases the *Mg*# of the upper mantle, as discussed in an earlier section (Structure formation in the magma ocean model), and the density reversal creates the upper cumulate layer—the lithosphere. It is worth emphasizing that the fast overturn rate implies that the large *Fe*# solid cumulates in the upper layer descend (as diapirs) into the bottom layers ($\gtrsim 400$ km depth), where the higher viscosity slows their eventual descent into the lower mantle.

The much slower overturn rate of the lower portion of the upper mantle (depth >400 km) in the presence of a lithosphere layer leads to the formation of the asthenosphere and the LVZ layer. As discussed in an earlier section (Origin of LVZ and the asthenosphere), upwelling from the deeper parts of the upper mantle brings water-bearing wadsleyite and ringwoodite to shallower depths of 220 – 250 km. The melt generated in the upwelling mantle, being more buoyant, rises to appear as a conductive LVZ layer under the lithosphere whose impermeable assemblage becomes a barrier, trapping the melt. The restite of this partial melting becomes the asthenosphere. Our analysis shows that the lithosphere formed before the asthenosphere. It also strongly suggests that the gravitational overturn of a solidified upper mantle creates a stratified structure that can support plate tectonics.

## CONCLUSIONS

The Earth is believed to have experienced at least one episode of large-scale melting because of the Moon-forming impact at ~4.5 Ga. The resulting evolution of the magma ocean (MO) to a layered convecting mantle, remains a complex theoretical problem (Solomatov, 2015; Schaefer and Elkins-Tanton, 2018). Fractionation of the magma ocean has been shown to lead to gravitationally unstable cumulate layers with density decreasing with increasing depth. A large-scale overturn after the solidification of magma ocean is known to form a stably stratified mantle that is geologically dead (Elkins-Tanton, 2012; Korenaga, 2021). We have proposed a preliminary model for the evolution of the gravitationally unstable state consistent with existing petrological, mineralogical, and experimental evidence. We have theoretically analyzed the dynamics of gravitational overturn in the magma ocean with a partial melt to a depth of $\lesssim$400 km and a rheological transition to a solid below this depth. We have shown that small-scale gravitational overturn dynamics have two very different timescales, with faster dynamics at shallower depths and significantly slower dynamics at greater ($\gtrsim$ 400 km) depths. At shallower depths, crystals of olivine, along with pyroxene and garnet, formed the lithosphere (~4.4 Ga). At the same time, the coexisting melt crystallized into the mafic crust over the lithosphere. The overlying mafic layer, melted by the heat flux from below, formed the felsic melt of TTG composition that solidified to give rise to an early continental crust of the Hadean age (4.2 – 4.02 Ga). The slower dynamics at depths $\gtrsim$ 400 km are argued to create a more homogeneous asthenosphere and a zone of partial melt – the low-velocity zone. The conductive layer of the LVZ below the lithosphere is a product of the partial melting of the mantle TZ emplaced from 410 km to 220 – 250 km. The residual material or restite formed the asthenosphere (~ 4.3 Ga). We propose the mechanism of mantle upwelling, coupled with the topographic rise of the crust by TTG formation, whereby TZ material was emplaced to a shallower depth of 220–250 km, where partial melting was enhanced by water ($OH^-$) released from the TZ minerals, wadsleyite, and ringwoodite when they transformed to olivine. The density reversal due to gravitational overturn changes the upper mantle's pressure profile and repositions transition zone discontinuities to 410 km and 660 km. Thus, our preliminary analysis shows that the magma ocean model leads to upper mantle structures supporting modern-day plate tectonics.

## ACKNOWLEDGMENTS

We thank Dr Om Prakash Pandey, Chief Editor, JIGU for his invitation to write this article. We thank Chris Hawkesworth and Nicholas Arndt for their comments on an earlier version of this manuscript.

### Author Credit Statement

Prashant Sharma: Conceptualization, methodology, formal analysis, and writing (original draft and edits). Ram S. Sharma: Conceptualization, methodology, writing (original draft and edits).

### Data Availability

All data generated during this study are derived from equations included in this published article. External data files used in this paper are available at (Ballmer et al., 2017).

### Compliance With Ethical Standards

The authors declare no conflict of interest and adhere to copyright norms.

## REFERENCES

Abe, Y., 1993. Physical state of the very early Earth. Lithos, 30 (3–4), 223–235.

Agee, C.B. and Walker, D., 1993. Olivine flotation in mantle melt. Earth Planet. Sci. Lett., 114 (2–3), 315–324.

Anderson, D.L., 2007. New Theory of the Earth. Cambridge University Press.

Andrault, D., Pesce, G., Manthilake, G., Monteux, J., Bolfan-Casanova, N., Chantel, J., Novella, D., Guignot, N., King, A., Itié, J.-P. and Hennet, L., 2018. Deep and persistent melt layer in the Archaean mantle. Nature Geoscience, 11 (2), 139–143.

Arndt, N., 2013. Formation and Evolution of the Continental Crust. Geochem. Perspectives, 2 (3), 405–533.

Ballmer, M.D., Lourenço, D.L., Hirose, K., Caracas, R. and Nomura, R., 2017. Reconciling magma-ocean crystallization models with the present-day structure of the Earth's mantle. Geochem. Geophys. Geosyst., 18 (7), 2785–2806.

Bolfan-Casanova, N., 2005. Water in the Earth's mantle. Mineralogical Magazine, 69 (3), 229–257.

Bolrão, D.P., Ballmer, M.D., Morison, A., Rozel, A.B., Sanan, P., Labrosse, S. and Tackley, P.J., 2021. Timescales of chemical equilibrium between the convecting solid mantle and over- and underlying magma oceans. Solid Earth, 12 (2), 421.

Boukaré, C.-E., Ricard, Y. and Fiquet, G., 2015. Thermodynamics of the MgO-FeO-SiO2 system up to 140 GPa: Application to the crystallization of Earth's magma ocean. J. Geophys. Res. Solid Earth, 120 (9), 6085–6101.

Boukaré, C.-E., Parmentier, E.M. and Parman, S.W., 2018. Timing of mantle overturn during magma ocean solidification. Earth Planet. Sci. Lett., 491, 216–225.

Bowring, S.A. and Williams, I.S., 1999. Priscoan (4.00-4.03 Ga) orthogneisses from northwestern Canada. Contr. Mineralogy and Petrology, 134 (1), 3–16.

Boyd, F.R., 1989. Compositional distinction between oceanic and cratonic lithosphere. Earth Planet. Sci. Lett., 96 (1–2), 15–26.

Caracas, R., Hirose, K., Nomura, R. and Ballmer, M.D., 2019. Melt–crystal density crossover in a deep magma ocean. Earth Planet. Sci. Lett., 516, 202–211.

Carlson, R.W., Garnero, E., Harrison, T.M., Li, J., Manga, M., McDonough, W.F., Mukhopadhyay, S., Romanowicz, B., Rubie, D., Williams, Q. and Zhong, S., 2014. How Did Early Earth Become Our Modern World? Annual Rev. Earth Planet. Sci., 42 (1), 151–178.

Chandrasekhar, S., 1961. Hydrodynamic and Hydromagnetic Stability. Clarendon Press.

Chudinovskikh, L. and Boehler, R., 2001. High-pressure polymorphs of olivine and the 660-km seismic discontinuity. Nature, 411 (6837), 574–577.

Conrad, C.P. and Molnar, P., 1997. The growth of Rayleigh–Taylor-type instabilities in the lithosphere for various rheological and density structures. Geophys. J. Int., 129 (1), 95–112.

Deng, J. and Lee, K.K.M., 2017. Viscosity jump in the lower mantle inferred from melting curves of ferropericlase. Nature Comm., 8 (1), 1997.

Dhuime, B., Wuestefeld, A. and Hawkesworth, C.J., 2015. Emergence of modern continental crust about 3 billion years ago. Nature Geoscience, 8 (7), 552–555.

Dixon, J.E., Dixon, T.H., Bell, D.R. and Malservisi, R., 2004. Lateral variation in upper mantle viscosity: role of water. Earth Planet. Sci. Lett., 222 (2), 451–467.

Drake, M.J., 2000. Accretion and primary differentiation of the Earth: a personal journey. Geochim. Cosmochim. Acta, 64 (14), 2363–2369.

Elkins-Tanton, L.T., 2008. Linked magma ocean solidification and atmospheric growth for Earth and Mars. Earth Planet. Sci. Lett., 271 (1–4), 181–191.

Elkins-Tanton, L.T., 2012. Magma Oceans in the Inner Solar System. Annual Rev. Earth Planet. Sci., 40 (1), 113–139.

Elkins-Tanton, L.T., Parmentier, E.M. and Hess, P.C., 2003. Magma ocean fractional crystallization and cumulate overturn in terrestrial planets: Implications for Mars. Meteoritics & Planet. Sci., 38 (12), 1753–1771.

Fei, Y., Mao, H., Shu, J., Parthasarathy, G., Bassett, W.A. and Ko, J., 1992. Simultaneous high-P, high-T X ray diffraction study of β-(Mg,Fe)2SiO4 to 26 GPa and 900 K. J. Geophys. Res., Solid Earth, 97 (B4), 4489–4495.

Férot, A. and Bolfan-Casanova, N., 2012. Water storage capacity in olivine and pyroxene to 14GPa: Implications for the water content of the Earth's upper mantle and nature of seismic discontinuities. Earth Planet. Sci. Lett., 349–350, 218–230.

Fiquet, G., Auzende, A.L., Siebert, J., Corgne, A., Bureau, H., Ozawa, H. and Garbarino, G., 2010. Melting of Peridotite to 140 Gigapascals. Science, 329, 1516–1518.

Foley, B.J., Bercovici, D. and Elkins-Tanton, L.T., 2014. Initiation of plate tectonics from post-magma ocean thermochemical convection. J. Geophys. Res., Solid Earth, 119 (11), 8538–8561.

Froude, D.O., Ireland, T.R., Kinny, P.D., Williams, I.S., Compston, W., Williams, I.R. and Myers, J.S., 1983. Ion microprobe identification of 4,100–4,200 Myr-old terrestrial zircons. Nature, 304 (5927), 616–618.

Garnero, E.J. and McNamara, A.K., 2008. Structure and Dynamics of Earth's Lower Mantle. Science, 320 (5876), 626–628.

Green, D.H. and Ringwood, A.E., 1970. Mineralogy of peridotite compositions under upper mantle conditions. Phys. Earth Planet. Int., 3, 359–371.

Grotzinger, J. and Jordan, T.H., 2019. Understanding Earth. Macmillan.

Harrison, T.M., 2009. The Hadean Crust: Evidence from > Ga Zircons. Annual Rev. Earth Planet. Sci., 37 (1), 479–505.

Hauri, E., Gaetani, G. and Green, T., 2006. Partitioning of water during melting of the Earth's upper mantle at H2O-undersaturated conditions. Earth Planet. Sci. Lett., 248 (3–4), 715–734.

Hawkesworth, C.J., Cawood, P.A., Dhuime, B. and Kemp, T.I.S., 2017. Earth's Continental Lithosphere Through Time. Annual Rev. Earth Planet. Sci., 45 (1), 169–198.

Herzberg, C. and Rudnick, R., 2012. Formation of cratonic lithosphere: An integrated thermal and petrological model. Lithos, 149, 4–15.

Hirose, K., 2002. Phase transitions in pyrolitic mantle around 670-km depth: Implications for upwelling of plumes from the lower mantle. J. Geophys. Res., Solid Earth, 107 (B4), ECV 3-1-ECV 3-13.

Hirschmann, M.M., 2010. Partial melt in the oceanic low velocity zone. Phys. Earth Planet. Int., 179 (1–2), 60–71.

Hirschmann, M.M. and Dasgupta, R., 2009. The H/C ratios of Earth's near-surface and deep reservoirs and consequences for deep Earth volatile cycles. Chem. Geol., 262 (1–2), 4–16.

Hirschmann, M.M., Asimow, P.D., Ghiorso, M.S. and Stolper, E.M., 1999. Calculation of Peridotite Partial Melting from Thermodynamic Models of Minerals and Melts. III. Controls on Isobaric Melt Production and the Effect of Water on Melt Production. J. Petrology, 40 (5), 831–851.

Hirschmann, M.M., Aubaud, C. and Withers, A.C., 2005. Storage capacity of H2O in nominally anhydrous minerals in the upper mantle. Earth Planet. Sci. Lett., 236 (1–2), 167–181.

Hofmann, A.W., 1988. Chemical differentiation of the Earth: the relationship between mantle, continental crust, and oceanic crust. Earth Planet. Sci. Lett., 90 (3), 297–314.

Hofmann, A.W., 2007. Treatise on Geochemistry, 1–44.

Hopkins, M.D., Harrison, T.M. and Manning, C.E., 2010. Constraints on Hadean geodynamics from mineral inclusions in > 4Ga zircons. Earth Planet. Sci. Lett., 298 (3–4), 367–376.

Hua, J., Fischer, K.M., Becker, T.W., Gazel, E. and Hirth, G., 2023. Asthenospheric low-velocity zone consistent with globally prevalent partial melting. Nature Geoscience, 16 (2), 175–181.

Hyung, E. and Jacobsen, S.B., 2020. The 142Nd/144Nd variations in mantle-derived rocks provide constraints on the stirring rate of the mantle from the Hadean to the present. Proc. National Acad. Sci., 117 (26), 14738–14744.

Kamber, B.S., 2015. The evolving nature of terrestrial crust from the Hadean through the Archaean, into the Proterozoic. Precamb. Res., 258, 48–82.

Karato, S., 2012. On the origin of the asthenosphere. Earth Planet. Sci. Lett., 321–322, 95–103.

Kemp, A.I.S., Wilde, S.A., Hawkesworth, C.J., Coath, C.D., Nemchin, A., Pidgeon, R.T., Vervoort, J.D. and DuFrane, S.A., 2010. Hadean crustal evolution revisited: New constraints from Pb–Hf isotope systematics of the Jack Hills zircons. Earth Planet. Sci. Lett., 296 (1–2), 45–56.

Khazan, Y., 2010. Melt segregation and matrix compaction: the mush continuity equation, compaction/segregation time, implications. Geophys. J. Int., 183 (2), 601–610.

Korenaga, J., 2021. Hadean geodynamics and the nature of early continental crust. Precamb. Res., 359, 106178.

Kranendonk, M.V., 2010. Two types of Archean continental crust: Plume and plate tectonics on early Earth. American J. Sci., 310, 1187–1209.

Kranendonk, M.J.V., Smithies, R.H., Hickman, A.H. and Champion, D.C., 2007. Review: secular tectonic evolution of Archean continental crust: interplay between horizontal and vertical processes in the formation of the Pilbara Craton Australia. Terra Nova, 19 (1), 1–38.

Kushiro, I., 1969. The System Forsterite-Diopside-Silica with and Without Water at High Pressures. American J. Science, 267-A, 269–294.

Labrosse, S., Hernlund, J.W. and Coltice, N., 2007. A crystallizing dense magma ocean at the base of the Earth's mantle. Nature, 450 (7171), 866–869.

Lambert, I.B. and Wyllie, P.J., 1970. Low-Velocity Zone of the Earth's Mantle: Incipient Melting Caused by Water. Science, 169 (3947), 764–766.

Landau, L.D. and Lifshitz, E.M., 1987. Fluid Mechanics: Course of Theoretical Physics Volume 6. Second. Elsevier.

Lebrun, T., Massol, H., Chassefière, E., Davaille, A., Marcq, E., Sarda, P., Leblanc, F. and Brandeis, G., 2013. Thermal evolution of an early magma ocean in interaction with the atmosphere. J. Geophys. Res., Planets, 118 (6), 1155–1176.

Lee, C.-T.A., Luffi, P. and Chin, E.J., 2011. Building and Destroying Continental Mantle. Annual Rev. Earth Planet. Sci., 39 (1), 59–90.

Lev, E. and Hager, B.H., 2008. Rayleigh–Taylor instabilities with anisotropic lithospheric viscosity. Geophys. J. Int., 173 (3), 806–814.

Liebske, C., Corgne, A., Frost, D.J., Rubie, D.C. and Wood, B.J., 2005. Compositional effects on element partitioning between Mg-silicate perovskite and silicate melts. Contr. Mineralogy and Petrology, 149 (1), 113–128.

Maurice, M., Tosi, N., Samuel, H., Plesa, A., Hüttig, C. and Breuer, D., 2017. Onset of solid-state mantle convection and mixing during magma ocean solidification. J. Geophys. Res., Planets, 122 (3), 577–598.

McFarlane, E.A., Drake, M.J. and Rubie, D.C., 1994. Element partitioning between Mg-perovskite, magnesiowüstite, and silicate melt at conditions of the Earth's mantle. Geochim. Cosmochim. Acta, 58 (23), 5161–5172.

Mei, S., Bai, W., Hiraga, T. and Kohlstedt, D., 2002. Influence of melt on the creep behavior of olivine-basalt aggregates under hydrous conditions. Earth Planet. Sci. Lett., 201, 491–507.

Mierdel, K., Keppler, H., Smyth, J.R. and Langenhorst, F., 2007. Water Solubility in Aluminous Orthopyroxene and the Origin of Earth's Asthenosphere. Science, 315 (5810), 364–368.

Mikaelian, K.O., 1996. Rayleigh-Taylor instability in finite-thickness fluids with viscosity and surface tension. Phys. Rev. E, 54 (4), 3676–3680.

Miyazaki, Y. and Korenaga, J., 2019. On the Timescale of Magma Ocean Solidification and Its Chemical Consequences: 2. Compositional Differentiation Under Crystal Accumulation and Matrix Compaction. J.f Geophys. Res., Solid Earth, 124 (4), 3399–3419.

Mojzsis, S.J., Cates, N.L., Caro, G., Trail, D., Abramov, O., Guitreau, M., Blichert-Toft, J., Hopkins, M.D. and Bleeker, W., 2014. Component geochronology in the polyphase ca. 3920 Ma Acasta Gneiss. Geochim. Cosmochim. Acta, 133, 68–96.

Monteux, J., Andrault, D., Guitreau, M., Samuel, H. and Demouchy, S., 2020. A mushy Earth's mantle for more than 500 Myr after the magma ocean solidification. Geophys. J. Int., 221 (2), 1165–1181.

Mosenfelder, J.L., Asimow, P.D., Frost, D.J., Rubie, D.C. and Ahrens, T.J., 2009. The MgSiO3 system at high pressure: Thermodynamic properties of perovskite, postperovskite, and melt from global inversion of shock and static compression data. J. Geophys. Res., Solid Earth, 114 (B1).

Moyen, J.-F. and Martin, H., 2012. Forty years of TTG research. Lithos, 148, 312–336.

Nabiei, F., Badro, J., Boukaré, C.-É., Hébert, C., Cantoni, M., Borensztajn, S., Wehr, N. and Gillet, P., 2021. Investigating Magma Ocean Solidification on Earth Through Laser-Heated Diamond Anvil Cell Experiments. Geophys. Res. Lett., 48 (12), e2021GL092446.

Ohtani, E., Suzuki, A. and Kato, T., 1993. Flotation of Olivine in the Peridotite Melt at High Pressure. Proc. Japan Acad., Series B, 69 (2), 23–28.

Ohtani, E., Nagata, Y., Suzuki, A. and Kato, T., 1995. Melting relations of peridotite and the density crossover in planetary mantles. Chem. Geol., 120 (3–4), 207–221.

Philpotts, A.R. and Ague, J.J., 2022. Principles of Igneous and Metamorphic Petrology. 3rd ed. Cambridge: Cambridge University Press.

Pilchin, A. and Eppelbaum, L.P., 2008. The Early Earth and formation of Lithosphere. Nova Science Publishers Inc. New York.

Piriz, A.R., Cortázar, O.D., Cela, J.J.L. and Tahir, N.A., 2006. The rayleigh-taylor instability. American J. Phys., 74 (12), 1095–1098.

Poirier, J.-P., 2000. Introduction to the Physics of the Earth's Interior. 2nd ed. Cambridge: Cambridge University Press.

Reese, C.C. and Solomatov, V.S., 2006. Fluid dynamics of local martian magma oceans. Icarus, 184 (1), 102–120.

Ringwood, A.E., 1975. Composition and Petrology of the Earth's Mantle. Mc Graw Hill.

Rozel, A.B., Golabek, G.J., Jain, C., Tackley, P.J. and Gerya, T., 2017. Continental crust formation on early Earth controlled by intrusive magmatism. Nature, 545 (7654), 332–335.

Santosh, M., Arai, T. and Maruyama, S., 2017. Hadean Earth and primordial continents: The cradle of prebiotic life. Geosci. Front., 8 (2), 309–327.

Schaefer, L. and Elkins-Tanton, L.T., 2018. Magma oceans as a critical stage in the tectonic development of rocky planets. Phil. Trans. Royal Society A: Mathematical, Physical and Engineering Sciences, 376 (2132), 20180109.

Sharma, R.S., 2016. Metamorphic Petrology. Geological Society of India.

Sifré, D., Gardés, E., Massuyeau, M., Hashim, L., Hier-Majumder, S. and Gaillard, F., 2014. Electrical conductivity during incipient melting in the oceanic low-velocity zone. Nature, 509 (7498), 81–85. extra

Solomatov, V., 2015. Magma Oceans and Primordial Mantle Differentiation. In: G. Schubert, ed. Amsterdam, The Netherlands: Elsevier, 81–104.

Solomatov, V.S. and Stevenson, D.J., 1993. Nonfractional crystallization of a terrestrial magma ocean. J. Geophys. Res., Planets, 98 (E3), 5391–5406.

Solomon, S.C., 1979. Formation, history and energetics of cores in the terrestrial planets. Phys. Earth Planet. Int., 19 (2), 168–182.

Stixrude, L., Koker, N. de, Sun, N., Mookherjee, M. and Karki, B.B., 2009. Thermodynamics of silicate liquids in the deep Earth. Earth Planet. Sci. Lett., 278 (3–4), 226–232.

Stofan, E.R., Smrekar, S.E., Bindschadler, D.L. and Senske, D.A., 1995. Large topographic rises on Venus: Implications for mantle upwelling. J. Geophys. Res., 100 (E11), 23317.

Stolper, E., Walker, D., Hager, B.H. and Hays, J.F., 1981. Melt segregation from partially molten source regions: The importance of melt density and source region size. J. Geophys. Res., Solid Earth, 86 (B7), 6261–6271.

Takahashi, E., 1986. Melting of a dry peridotite KLB-1 up to 14 GPa: Implications on the Origin of peridotitic upper mantle. J. Geophys. Res., 91 (B9), 9367.

Taylor, S.R. and McLennan, S.M., 1995. The geochemical evolution of the continental crust. Rev. Geophys., 33 (2), 241.

Tonks, W.B. and Melosh, H.J., 1992. Magma Ocean Formation Due to Giant Impacts. In: Physics and Chemistry of Magma Oceans from 1 Bar to 4 Mbar. 66.

Turcotte, D.L. and Schubert, G., 2002. Geodynamics. 2nd ed. Cambridge: Cambridge University Press.

Weng, Y.-H. and Presnall, D.C., 2001. The System Diopsie – Forsterite – Enstatite at 5.1 GPa: A Ternary Model for Melting of the Mantle. The Canadian Mineralogist, 39 (2), 299–308.

Wetherill, G.W., 1990. Formation of the earth. Annual Rev. Earth Planet. Sci., 18, 205–256.

Wilde, S.A., Valley, J.W., Peck, W.H. and Graham, C.M., 2001. Evidence from detrital zircons for the existence of continental crust and oceans on the Earth 4.4 Gyr ago. Nature, 409 (6817), 175–178.

Windley, B.F., Kusky, T. and Polat, A., 2021. Onset of plate tectonics by the Eoarchean. Precamb. Res., 352, 105980.

Wood, J.A., Dickey, Jr., J.S., Marvin, U.B. and Powell, B.N., 1970. Lunar anorthosites and a geophysical model of the moon. Geochim. Cosmochim. Acta Supplement, 1, 965.

Wyllie, P.J., 1981. Plate tectonics and magma genesis. Geologische Rundschau, 70, 128–153.

Zhang, Y., Sekine, T., Lin, J., He, H., Liu, F., Zhang, M., Sato, T., Zhu, W. and Yu, Y., 2018. Shock Compression and Melting of an Fe-Ni-Si Alloy: Implications for the Temperature Profile of the Earth's Core and the Heat Flux Across the Core-Mantle Boundary. J. Geophys. Res., Solid Earth, 123 (2), 1314–1327.

Received on:18-07-2024; Revised on: 29-10-2024; Accepted on: 30-10-2024